Journal of Intelligent and Connected Vehicles
2023, **6**(2): 79–90
https://doi.org/10.26599/JICV.2023.9210006

Research Article

Anisotropy safety potential field model under intelligent and connected vehicle environment and its application in car-following modeling

Haozhan Ma, Bocheng An, Linheng Li, Zhi Zhou, Xu Qu, Bin Ran✉

School of Transportation, Southeast University, Nanjing 210096, China

Received: November 26, 2022; Revised: February 9, 2023; Accepted: February 13, 2023

ABSTRACT: Potential field theory, as a theory that can also be applied to vehicle control, is an emerging risk quantification approach to accommodate the connected and self-driving vehicle environment. Vehicles have different risk impact effects on other road participants in each direction under the influence of road rules. This variability exhibited by vehicles in each direction is not considered in the previous potential field model. Therefore, this paper proposed a potential field model that takes the anisotropy of vehicle impact into account: (1) introducing equivalent distances to separate the potential field area in the different directions before and after the vehicle; (2) introducing co-virtual forces to characterize the effect of the side-by-side travel phenomenon on vehicle car-following travel; (3) introducing target forces and lane resistance, which regress the control of desired speed to control the acceptable risk of drivers. The Next Generation Simulation (NGSIM) dataset is used in this study to create the model's initial parameter values based on the artificial swarm algorithm. The simulation findings indicate that when the vehicle is given the capacity to perceive the surrounding traffic environment, the suggested the anisotropic safety potential field model (ASPFM) performs better in terms of driving safety.

KEYWORDS: connected and automated vehicles, car-following model, potential field, anisotropy, trajectory estimation

1 Introduction

Intelligent information interaction between vehicles and X (vehicles, people, clouds, roads, etc.) may be achieved by outfitting powerful actuators, onboard sensors, computing system, controllers, and other devices as well as incorporating contemporary communication and network technology (Xu et al., 2022). The car can drive in a way that is "safe, efficient, pleasant, and energy-saving" because of its sophisticated environment awareness, intelligent decision-making, collaborative control, and other features (Yuan et al., 2022; Zhu et al., 2022). Scientific risk quantification is a key building block for the development of intelligent and connected cars to improve safety. As a basic microscopic behavior, the car-following process accounts for the highest percentage of vehicle movements. Previous car-following models aim to increase forecast accuracy and clarify its mechanism. These models blamed the leading car for the objective vehicle's acceleration, which led to poor performance in balancing comfort and safety (Gipps, 1981; Jiang et al., 2001).

The potential field model is distinctive because it measures risk. Additionally, the potential field model may take into account the effects of several vehicles at once by integrating field theory into the microscopic behavior modeling of cars. Fortunately, the potential field method is still gaining attention and used by academics in the microscopic control of vehicles, robot path planning, and navigation (Mac et al., 2016). Potential field theory was first introduced to other disciplines and excels in controlling mobile robots to avoid obstacles in real time (Khatib, 1986). Currently, potential field theory is receiving a significant amount of attention from academics in the subject of transportation, which can provide a more realistic picture of a wide range of risk quantification methods. What is more, academics also model the potential field of an obstacle for controlling an entity to avoid obstacles and perform the normal motion. Yu and Lu (2021) considered the effect of speed on safety and defined the potential field as ellipsoidal whose long axis always aligned with the speed direction to enhance the safety of the UAV against obstacles in the direction of motion. Similarly, Li et al. (2022) suggested an car-following model by introducing potential field theory, which can effectively reproduce the actual following process of the cars. Due to the use of the car-following pair, the car-following model they developed only verified the accuracy of the obstacle vehicle's impact on the rear objective vehicle, while the effect in other directions lacked verification. The artificial potential field (APF) fine-grained resistance approach was the foundation for the architecture. Huang et al. (2020) proposed a framework for motion planning and tracking in autonomous vehicles that involved dividing the driving area into a grid and assigning resistance values to each edge. The resulting travel path was determined based on these resistance values. The effectiveness of this framework was then verified through simulation experiments conducted using CarSim software. Liu et al. (2022) used a conditional variance autoencoder to provide candidate trajectories with probabilities based on driving risk maps and motion uncertainty trajectories, and used another module for accurate trajectory prediction. They constructed the vehicle driving risk maps, rather than measures of vehicles' impact on other road

✉ Corresponding author.
E-mail: bran@seu.edu.cn

participants. In summary, potential field theory has received a wide range of applications in traffic flow theory and has illustrated prominent advantages in continuously characterizing the road operating environment. The impact of yield rules, however, has been less considered in current research, making it difficult for models to accurately characterize realistic traffic phenomena.

The influence of conditions, such as yield rules and the operational status of vehicles in adjacent lanes on vehicles, causes vehicles to exhibit different effects on traffic elements in each direction. For example, when driving on the freeway, the high velocity of the vehicles causes small directional shifts to be accompanied by dramatic changes in trajectory. The air currents generated around the vehicles would interact with each other, further increasing the risk of accidents when traveling side-by-side (Fu and Fu, 2005). Not only the direct effect caused by the airflow, but prolonged side-by-side driving without implementing the appropriate acceleration and deceleration adversely affects the intention to overtake (Gunay, 2007). However, this is not considered in traditional potential field models, which only identify side-by-side vehicles as an essential influence factor in preventing lane changes. Although potential field models are a good representation of the interaction between vehicles traveling side by side, current potential field models do not extend this influence to the car-following process. This requires a model that can take into account multiple surrounding traffic elements simultaneously, rather than just the vehicles in front, for controlling the vehicles to move more safely.

In summary, there are still two important limitations of the existing car-following model: First, preceding potential field models failed to account for the simultaneous effects of multiple obstacle vehicles (in this paper, vehicles around the objective vehicle that prevent it from driving in a free-flowing state are referred to as obstacle vehicles). Despite its potential to explain the concurrent impact of multiple cars, prior potential models did not account for the impact of vehicles other than the leading vehicles. Secondly, extant models have failed to account for the anisotropic nature of vehicle impact, which arises from the interplay between yield rule and speed. The aforementioned attributions of these models impair their capacity to deliver a precise delineation of risk, thereby constituting a potential jeopardy to the realm of road safety. In this paper, we assume that all traffic elements can be detected in real time in the intelligent and connected environment. Therefore, we construct a model that can contain information about the operational status of multiple obstacle vehicles as required (the detailed description can be found in Section 4) to control the car-following process. This paper innovatively proposed the concept of co-virtual forces to characterize and describe the tendency of acceleration and deceleration arising from the state of vehicles in adjacent lanes. The created car-following model's parameters are calibrated using the artificial bee colony algorithm and real trajectory data from the Next Generation Simulation (NGSIM). Finally, the efficiency of the model in assuring driving safety is evaluated by comparing it with other typical models, such as the IDM.

The remaining content is arranged as follows: A review of earlier studies is provided in Section 2. The anisotropic safety potential field is developed based on the car-following process in Section 3. In Section 4, the suggested model is calibrated using the NGSIM dataset and used to the trajectory estimation validation. Finally, Section 5 contains the findings.

2 Literature review

Numerous efforts have been devoted to quantifying the risk, primarily using two vastly different approaches. A large number of academics have adopted a number of numerical indicators to describe driving risk as a cornerstone of mobile vehicles. Although the assessment of risk varies slightly in different scenarios, the widely used safety metrics currently include the following two categories: evaluation based on spatial distance (gap distance involving neighboring vehicles) (Kometani and Sasaki, 1959; Yang et al., 2019); evaluation of vehicle travel safety based on speed and time (the most widely used one is time to collision (TTC)) (Lee, 1976). It is followed by various variants formed by improving on TTC, such as CSC (−1/TTC) (Jiao et al., 2021). However, these metrics are usually difficult to systematically evaluate the hazard level of two-dimensional scenarios. Furthermore, academics have come to the conclusion that accident incidence is a complicated system driven by a number of contributing elements, regardless of the method employed (Khattak et al., 2021; Zhao and Rao, 2021). Due to the non-directly observable nature of risk, some academics have built discrete choice models using data on traffic accidents or conflicts to verify the logic of risk measurement (Cheng et al., 2022; Wang et al., 2019). The application of such approaches is further constrained by the potential absence of crash data caused by the improvement in safety enhanced by connected and autonomous vehicles (Kim et al., 2020).

Along with high precision and a large sample of vehicle driving data, the 1990s saw the advent of data-driven vehicle microscopic control models (Li and Chen, 2017). In order to swiftly create the autonomous driving judgments, Masmoudi et al. (2021) initially employed YOLOv3 identification detection and then applied Q-learning and Deep Q-learning. To increase the accuracy and stability of the car-following model, Xing and Liu (2022) abstracted the vehicle following process as graph information and utilized graph neural networks to describe the game process between the intended driving status of the vehicle and the actual traffic state. Some academics have also developed simulation of the car-following model to map the following vehicle's acceleration from its speed, the vehicle headway, and the relative speed in a human-like manner in order to achieve homogeneity based on deep reinforcement learning (Zhu et al., 2018). To forecast the chance of making different decisions, these researches, however, did not take the relationship between risk perception and decision-making into consideration and instead simply searched for a few behavioral patterns that arose from a significant quantity of data. Further reducing the heterogeneity of mixed traffic flows requires the construction of models from human behavioral mechanisms (Lyu et al., 2022; Xu et al., 2022).

In order to endow vehicles with the ability to evaluate risk based on environmental cues, the potential field theory is frequently adopted as a cornerstone for decision-making (Zheng et al., 2018). Drivers make judgments about their conduct based on driving needs as they plot their trajectory and mobility, taking into account environmental limits and collision hazards in real time (Zhao et al., 2020). Several academics, therefore, have presented vehicle control models that are typically based on field theory and validated using real trajectory data. The assistance system presented by Noto et al. (2012) is based on a customized map that is thought to represent the driver's perception of environmental danger and was trained using naturalistic driving data to avoid obstacles. By using potential field values as a penalty function for vehicle path planning, some academics developed a vehicle controller that plans an optimal trajectory (Rasekhipour et al., 2017; Wang et al., 2019). On the basis of their previous research, Li et al. (2020a) proposed a unique approach to perceive risk and

provide warning strategy that can more precisely depict the real driving danger experienced by automobiles under various vehicle motion states. Taking into account the differences between scenario-based models and field theory-based models, a model that combines the properties of both types of models is created, and ten instances are chosen from Next Generation Simulation (NGSIM) for validating model (Tan et al., 2022). Similarly, potential fields have also been used to control ships, for example, Perera and Soares (2015) presented a vessel control model by vector dot and fork product under the condition of considering the randomness of the vessel and evaluated its effectiveness by the trajectory. The risk potential field theory-based microscopic traffic flow model may effectively describe the risk while driving, particularly in the intelligent and connected environment where motion states information of possible vehicles can be collected (Li et al., 2020b).

Despite the fact that the intensity of an obstacle vehicle's impact changes in all directions due to the speed attribute of vehicles, a limited quantity of academics worked on risk modeling for the anisotropy of vehicle impact. For example, Arun et al. (2023) created a framework based on the idea that the potential fields in each direction assume distinct values and include accident severity and occurrence risk. A limited quantity of academics worked on risk modeling for the anisotropy of vehicle impact, although established vehicle control approaches generally simplify this risk feature. Besides, in previous studies, potential field theory was applied in the form of "car-following pairs", which makes it impossible to measure the risk impact of multiple vehicles simultaneously. Hence, this paper focuses on the measurement of how road vehicle affects other vehicles and proposes a model that takes into account the anisotropy of multiple vehicles' impact.

3 Methodology

Anisotropy is a characteristic that causes traffic components moving in various directions to affect cars in different ways when governed by traffic laws. It is a property where traffic elements have different degrees of influence on vehicles in different directions even at equal distances. Although the potential field of a stationary obstacle is theoretically supposed to be a circle centered on itself, the effect of relative speed makes the degree of risk vary in different directions. That is, anisotropy is a figurative representation of the rules of the road on the driver's driving decisions.

This study illustrates the car-following process using the safety potential field and virtual forces. It is assumed that the road on which vehicles travel is perfectly horizontal without any height fluctuations. The direction from the outer lane to the inner lane is taken as the positive y-axis direction, while the vehicle moving direction is taken as the positive x-axis direction, and thus the coordinate system of this paper is determined. The coordinate system that serves as the foundation for this research is depicted schematically in Fig. 1. Additionally, the coordinate origin is not only as exhibited in Fig. 1.

3.1 Anisotropy safety potential field

As previously mentioned, anisotropy is a characteristic that can be observed in the coordinate system as distinct effects that occur along four directions. These effects include unequal impacts along the direction of vehicle travel and the lateral tangential direction, as well as asymmetric effects along the front and rear directions of vehicle travel. Moreover, when vehicles travel side-by-side, an additional variation in anisotropy can be observed, whereby those

Fig. 1 Coordinate system when the origin is outside the road.

on the inside of the road should accelerate, while those on the outside should decelerate.

3.1.1 Vehicle properties

ς is the virtual inertia, which is essentially a measure of how a vehicle affects other vehicles on the road. It is a measure of vehicle externality (Wang et al., 2015, 2016):

$$\varsigma = m \times \left(1.566 \times 10^{-14} \times v^{6.687} + 0.03345\right) \tag{1}$$

where m is the vehicle mass (throughout this paper, the two-dimensional (2D) projected area of the vehicle is used instead), and v is the velocity of vehicle. However, due to the difficulty of obtaining this parameter of vehicle mass, the area of the vehicle obtained from the vehicle's length and width is used as an alternative metric to characterize the effect of mass m.

The vehicle risk mass, denoted as $\boldsymbol{\tau}$, is defined as a measure of the impact caused by other elements in the road environment on the decision-making of the vehicle. Specifically, $\boldsymbol{\tau}$ is oriented perpendicular to the plane of travel and directed vertically upwards. By quantifying the potential risks associated with the surrounding environment, $\boldsymbol{\tau}$ can serve as a valuable metric for enhancing the safety and efficiency of vehicular travel. In other words, the vehicle risk mass is a measure of how much the vehicle is affected by external influences.

$$|\boldsymbol{\tau}| = me^{\eta v} \tag{2}$$

where η is the undetermined coefficient. The length and direction of $\boldsymbol{\tau}$ will be used to solve for the magnitude of the virtual force and the direction of the co-virtual force, respectively, as detailed in the following two sections.

3.1.2 Vehicle potential field

It is worth stating additionally that all objects generating potential fields are obstacles relative to the objective vehicle, which means that subjects of the vehicle potential fields are obstacle vehicles. The vehicle potential field is a model for measuring the impact of obstacle vehicles. This model uses equivalent distances (Li et al., 2022) to provide a measure of the variability in vehicle direction of travel and tangential effects:

$$|k| = \sqrt{\left(\frac{x - x_0}{g(v)}\right)^2 + (y - y_0)^4} \tag{3}$$

where $g(v)$ denotes a function, v represents the speed of obstacle vehicle, and x_0 and y_0 are the coordinates of objective vehicle. Furthermore, there are cases in real-world scenarios where the impact of the preceding vehicle has a much greater influence than that of the following vehicle. Additionally, there is an imbalance of usefulness in the vertical direction. For instance, traffic regulations dictate that a stationary vehicle only affects the vehicle approaching from behind, but not the vehicle that has already

清华大学出版社 Tsinghua University Press | IEEE

passed it. This property is also dependent on the speed of the obstacle vehicle: as the speed of the obstacle vehicle increases, its impact on vehicles in the negative direction of the x-axis decreases, while its effect on objective vehicle in the positive direction of the x-axis increases significantly.

To characterize this property, the equivalent distances in the front and rear directions of vehicle travel are distinguished. Specifically, two discount factors are introduced and the model hyperparameter is set to the road speed limit v_m: the potential field in the x-positive axis direction of obstacle vehicle grows with increasing the vehicle speed. In contrast, the potential field along the x-negative axis direction diminishes as the speed of the vehicle rises. The equivalent distance becomes

$$|k| = \begin{cases} \sqrt{\left[\dfrac{(x-x_0)\,\delta_1}{v_m - |v|}\right]^2 + (y-y_0)^4}, x < x_0 \\ \sqrt{\left[\dfrac{(x-x_0)\,\delta_2}{|v|}\right]^2 + (y-y_0)^4}, x \geqslant x_0 \end{cases} \tag{4}$$

where δ_1 and δ_2 are the undetermined coefficients. The δ_1 and δ_2 have significant implications for the potential field, and it is important to recognize that their range of applicability is limited to one-directional road conditions. Other scenarios may require different values, as the directional nature of the road results in differing impacts of the obstacle vehicle on the front and rear directions. The distinct impacts are reflected by the use of two disparate functions.

$$|\boldsymbol{E}_V| = r_1 \varsigma \frac{\mathrm{e}^{r_2 a \cos\theta}}{|k|^2} \tag{5}$$

where r_1 and r_2 are the undetermined coefficients and θ is the angle between the line connecting the two vehicles' center points and x-positive axis. $\boldsymbol{E}_V$ is oriented from the center point of the obstacle vehicle to the center point of the objective vehicle. Let the x-axis component be $\boldsymbol{E}_{Vx}$ and the y-axis component be $\boldsymbol{E}_{Vy}$.

Fig. 2 indicates the vehicle potential field generated as a result of this study. Fig. 2a showcases the rapid decay of the obstacle vehicle's impact on the objective vehicle in front as the distance between the two vehicles increases, particularly when the obstacle vehicle is moving at a low and uniform speed. In contrast, the obstacle vehicle's influence on the objective vehicle on the trailing side remains significant. Fig. 2c displays a substantial increase in the overall potential field size at high speeds due to the obstacle vehicle's higher velocity. Additionally, Figs. 2b and 2d reveal the substantial impact of acceleration and deceleration, respectively, on the potential field in the direction of travel. Given a risk mass of $\boldsymbol{\tau}$ for the objective vehicle and its corresponding vehicle risk potential field $\boldsymbol{E}_V$, the resulting virtual force can be expressed as Eq. (6):

$$\boldsymbol{F}_0 = \sum \boldsymbol{E}_V \times |\tau| \tag{6}$$

where $\boldsymbol{F}_0$ is the virtual force assumed by the objective vehicle. Equation (6) describes the virtual force acting on the objective vehicle in the presence of an obstacle vehicle, disregarding the impact of the yield rule. The direction of the virtual force is determined by the obstacle vehicle screening rules taken and the state of obstacle vehicles, while its magnitude is determined by both the obstacle vehicles and the objective vehicle.

3.1.3 *Co-virtual force*

In addition to the inhomogeneity of the effects in the front-to-back direction, the actual driving risk of the vehicle varies in the left and right directions to avoid side-by-side driving and achieve the generation of overtaking intentions. Therefore, in addition to the virtual repulsive force obtained by multiplying each field strength by $|\boldsymbol{\tau}|$ to obtain the virtual repulsive force to applied to the vehicle, each field strength introduced an additional generated second virtual force, named the co-virtual force.

Decomposed into the x-axis and y-axis directions, $\boldsymbol{F}_0$ produced by the vehicle potential field is merged into two virtual forces, $\boldsymbol{F}_{x0}$ and $\boldsymbol{F}_{y0}$, which are applied to the vehicle in different directions. To

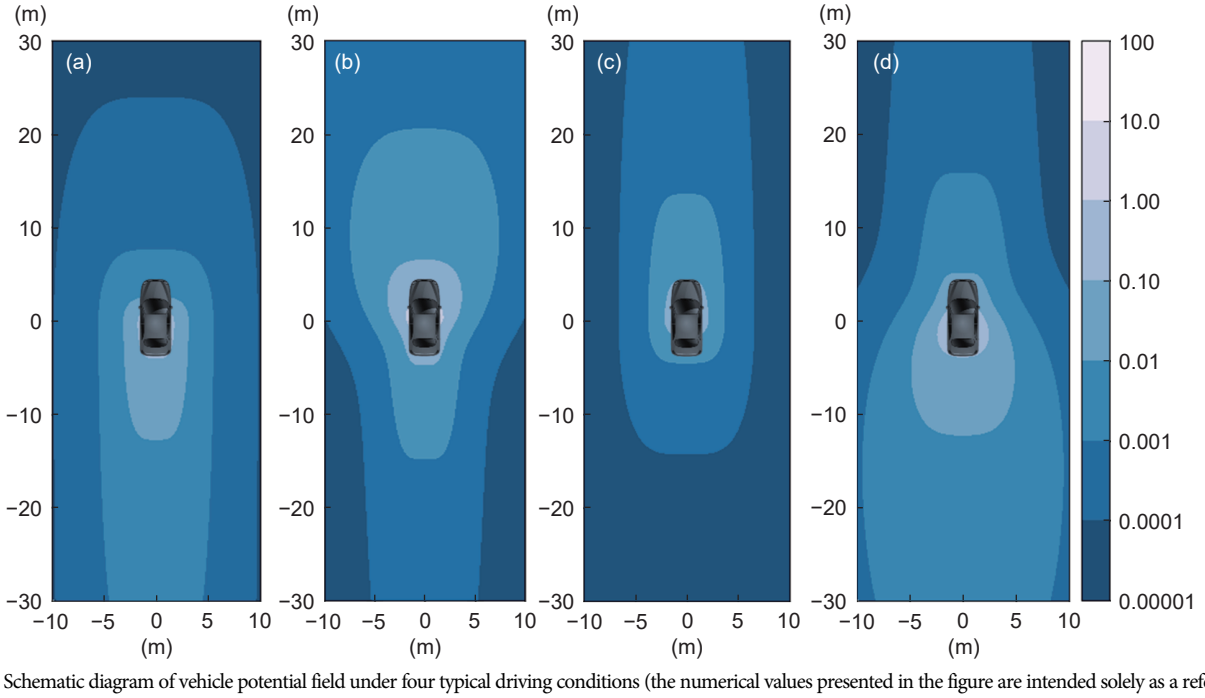

Fig. 2 Schematic diagram of vehicle potential field under four typical driving conditions (the numerical values presented in the figure are intended solely as a reference, with the exact values to be determined by the experimental section.): (a) when driving at low speed and $a = 0$; (b) when driving at low speed and $a > 0$; (c) when driving at a speed close to v_m and $a = 0$; (d) when driving at a speed close to v_m and $a < 0$.

assess the impact of the virtual force that propels a vehicle to accelerate or decelerate to avoid a potential obstacle, an avoidance coefficient β ($\beta > 0$) is introduced. The co-virtual force then can be computed as Eq. (7):

$$\boldsymbol{F}'_{y0} = \beta \boldsymbol{F}_{y0} \times \frac{\tau}{|\tau|} \tag{7}$$

where $\times$ represents the fork product of vectors. Eq. (7) can characterize the vehicle's propensity to decelerate in the presence of vehicles in the inside lane and to accelerate for overtaking in the presence of vehicles in the outside lane.

As shown in Fig. 3, the co-virtual force that results from applying a positive virtual force in the direction of the y-axis leads the vehicle to have a propensity to accelerate and vice versa. Co-virtual forces are also a reflection of how the vehicles is affected by the yield rules of the road. The co-virtual force generated by the virtual force applied in the y-axis direction is essentially a courtesy factor. It can be used as a safety redundancy parameter to characterize the degree of driver risk avoidance for side-by-side driving in the future intelligent and connected vehicle environment. Side-by-side driving can be further avoided by increasing the value of avoidance coefficient β.

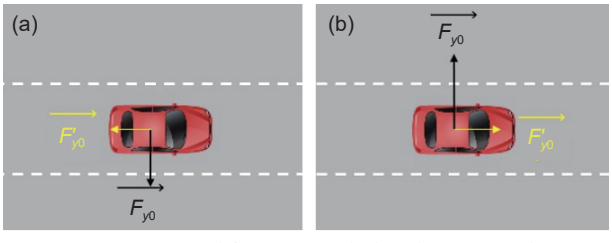

Fig. 3 (a) Synergistic virtual force generated when the y-axis resultant virtual force is positive; (b) synergistic virtual force generated when the y-axis resultant virtual force is negative.

The avoidance factor β is displayed in Fig. 4 when the vehicle is only influenced by a vehicle in the adjacent lane and no other traffic elements are influencing it. When the adjacent vehicle travels to the orange area, the potential field influence causes a tendency to slow down this vehicle. In contrast, when it travels to the green area, the potential field influence causes a tendency to accelerate this vehicle. In other words, the avoidance coefficient enlarges the area of arctanβ, enabling vehicles to anticipate whether to decelerate and yield or accelerate and overtake, thereby mitigating the hazards associated with side-by-side driving.

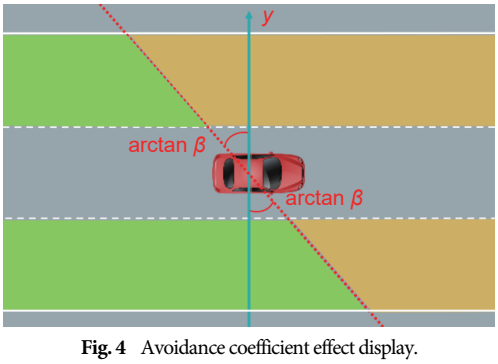

Fig. 4 Avoidance coefficient effect display.

3.2 Application in car-following process

The driver makes a decision to accelerate (decelerate), in a way that the acceptable risk is greater (less) than the risk currently assumed. In other words, acceleration is the dependable factor that must be verified to confirm the accuracy of risk quantification. The vehicle potential field, however, is not enough to be the entire constraint of vehicle travel, because the risk generated by obstacle vehicles is not all the elements considered by the driver, and the model proposed in this paper needs to be complemented by other elements.

3.2.1 *Goal force and lane resistance*

To make it possible to start the vehicle from rest in potential field/virtual force theory, the goal force $|\boldsymbol{F}_g| = f(d_g, t_g, ...)$ is introduced, where $\boldsymbol{F}_g$ is oriented in x-positive axis, d_g is the distance to the goal, and t_g is the desired time to reach the goal. Except for the final short distance near the destination, the target force $\boldsymbol{F}_g$ can be thought of as a constant throughout the journey. The degree to which the connected and autonomous vehicle will tolerate danger is another way to describe the goal force. The travel time and distance chosen by the user determines the acceptable level of risk. The vehicle decelerates when the risk is lower than the acceptable risk and vice versa.

The lane resistance $\boldsymbol{\xi}_i$ is introduced and given by

$$|\boldsymbol{\xi}_i| = \lambda_i m^{0.25} v + \zeta_i \tag{8}$$

where λ_i and ζ_i are the undetermined coefficients: λ_i represents the mapping of lane resistance as a function of speed, and ζ_i represents the constant lane resistance field from the outer to the inner lane i. The direction of lane resistance is the negative direction of the x-axis. This function can characterize the same mass case, the greater the speed, the greater the lane resistance. The objective vehicle has a greater acceleration at low speeds, while the acceleration tends to zero as it approaches the desired velocity. Besides, the resistance that an objective vehicle encounters in its lane at a given speed is directly proportional to its mass. Stated differently, a small vehicle can achieve a higher speed than a larger vehicle if both experience an equal magnitude of lane resistance. Furthermore, as i increases, λ_i decreases and ζ_i increases, which can characterize the lower speed cases where the vehicle is subjected to less resistance in the outer lane, and at higher speeds where the vehicle is subjected to less resistance in the inner lane. This expression is used to characterize and distinguish the desired velocity of different lanes.

The lane line constraint field strength $\boldsymbol{E}_\psi$ is introduced, with each lane sharing the same field strength $\boldsymbol{E}_\psi$ in the negative direction of the y-axis. Since the field strength that essentially acts as a constraint is the difference in field strength between the two adjacent lanes, the outermost lane is made to have a field strength of 0, i.e., $\boldsymbol{E}_\psi = 0$. The constrained virtual force of the lane line is $\boldsymbol{\psi} = |\boldsymbol{\tau}| \cdot \boldsymbol{E}_\psi$. One should note that since the lane line acts as a constraint on its decision to change lanes or not, the constraining virtual force does not act on the vehicle.

3.2.2 *Transforming risk into acceleration*

The virtual forces and co-virtual forces are combined again and then decomposed on the coordinate axes to obtain the virtual force $\boldsymbol{F}_x, \boldsymbol{F}_y$ applied in the objective vehicle.

The acceleration of the objective vehicle ($\boldsymbol{a}_x$) is determined when there is only interaction between different vehicles:

$$\boldsymbol{a}_x = \frac{\boldsymbol{F}_x}{m} = \left[\sum \left(\boldsymbol{E}_{Vx} + \beta \boldsymbol{E}_{Vy} \times \frac{\boldsymbol{\tau}}{|\boldsymbol{\tau}|}\right)\right] e^{\eta v} + \frac{\boldsymbol{F}_g + \boldsymbol{\xi}_i}{m} \tag{9}$$

As can be seen from Eq. (9), the lane resistance constant ζ_i only

清華大学出版社 Tsinghua University Press | IEEE

measures the difference between adjacent lanes, but not the lane resistance itself. Hence, the lane resistance constant ζ_i is assigned a value of 0 when considering a particular lane i in isolation, as opposed to comparing multiple lanes. The Anisotropic Safety Potential Field Model (ASPFM) presented in this study comprises all of the aforementioned equations combined.

4 Model validation

4.1 Parameter calibration

4.1.1 Data preparation

A connected and autonomous vehicle can make rational decisions even when it is challenging for a human driver to pay attention to the status of all the obstacle vehicles at once. This leads to the fact that human driver data is not well suitable to be interpreted by ASPFM. It should be emphasized, nevertheless, that ASPFM has a lot of latitudes to further tailor the anisotropic potential field's properties to the needs. Therefore, to make the initial values of the parameters reasonable, this paper uses actual data for the initial values of the parameter calibration of the model. The NGSIM dataset was selected with 4 lanes in both directions. Vehicle data from the outermost lane (lane 5) was utilized for parameter calibration.

As in the real scenario, the driver travels concerning the approaching vehicle and is not sensitive to vehicles obscured by the obscuring approaching vehicle. For parameter calibration, the driving states of the objective vehicle as well as the obstacle vehicles in a total of 5 vehicles during the vehicle travel are selected as a model parameter input node in this study (Fig. 5). Specifically, data with the objective vehicle in lane 5 and the presence of four obstructed vehicles around it are filtered out. The dataset was sliced every 3 frames, i.e., 0.12 s, and the acceleration was predicted for the next slice for each of the different car-following models. All data were sliced at 0.12 s intervals, and a total of 5 vehicles at each moment are used as an input node. Finally, 8,641 pieces of data that could be used for parameter calibration were selected. Each state parameter of the objective vehicle and the obstacle vehicles is input, including global coordinates, speed, acceleration and 2D projected area of vehicles. If an adjacent vehicle still exceeds the distance determination threshold, it is expected that the obstacle vehicle will not have a significant impact on the objective vehicle.

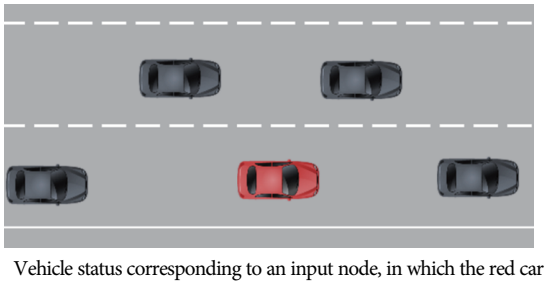

Fig. 5 Vehicle status corresponding to an input node, in which the red car is an objective vehicle and the black cars are obstacle vehicles.

Although measurements of acceleration are provided in the dataset, the principle of video data extraction results in acceleration not being a directly measured variable. Furthermore, due to the validity of two decimal places, the acceleration takes a high proportion of error float and is therefore only used as one of the variables in the potential field modeling.

4.1.2 Calibration algorithm

This study calibrates the parameters using the artificial bee colony algorithm. In Fig. 6, the processes involved in putting the artificial bee colony algorithm into practice are shown.

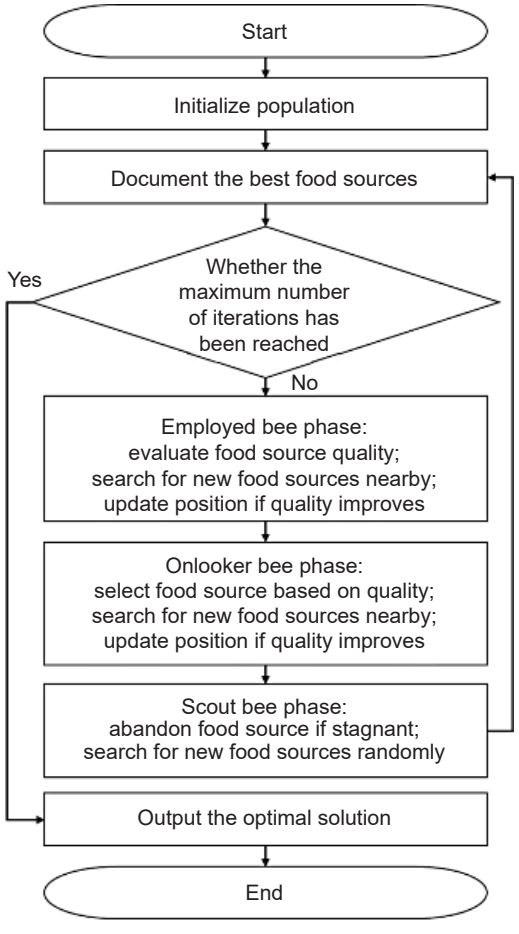

Fig. 6 Artificial bee colony algorithm flowchart.

Even with the drawbacks of poor population diversity in the late stages of evolution, low convergence accuracy, slow convergence, and the propensity to settle into local optimum solutions, the artificial bee colony algorithm, with few control parameters, is simple to implement and computationally concise. The artificial bee colony algorithm plays an important role in the swarm intelligence algorithm for solving continuum parameters.

4.1.3 Parameter calibration results

Python 3.10 was selected as the version to utilize in this investigation, and an i5-11300 computer processor was employed. Root mean square error (RMSE) is selected to be the assessment and validation index for the parameter calibration and its specific expression is

$$\mathrm{RMSE} = \sqrt{\frac{\sum_{i=1}^{n}\left(x_i - \widehat{x}_i\right)^2}{n}} \tag{10}$$

Table 1 displays the calibration results of model parameters in this study. The results of the parameter calibration for the other models are shown in Table 2.

To compare the models, the Optimal Velocity Model (OVM), Full Velocity Difference Model (FVD), Intelligent Driver Model (IDM), and Driving Risk Potential Field Model (DRPFM, Li

Table 1 Parameter calibration results of ASPFM

Parameter	Value
η	0.283
λ_i	0.755
δ_1	6.125
δ_2	13.216
r_1	4.030
r_2	0.664
$\lvert \boldsymbol{F}_g \rvert$	15.095
β	6.001

Table 2 Parameter calibration results of OVM, FVD, IDM, and DRPFM

Model	Parameter	Value
OVM	α_{OVM}	0.016
	v_{max}	25.369
	h_c	11.316
FVD	V_1	14.282
	V_2	21.097
	C_1	0.971
	C_2	8.527
	λ	0.161
	κ	0.006
IDM	v_{free}	23.328
	a	1.001
	b	6.458
	s_0	3.283
	T	0.300
DRPFM	v_0^{α}	28.487
	δ	6.520
	a_{max}	0.877
	λ	0.240
	α_{DRPFM}	−0.488
	β_1	−0.280
	β_2	0.040
	τ	4.001

et al., 2022) were selected for parameter calibration under the same dataset and the calibration results were compared. The size of the RMSE values could reveal a model's level of accuracy. The RMSE results for the five different models are as follows: ASPFM model 0.004177, OVM model 0.003127, FVD model 0.002952, IDM model 0.004738, and DRPFM model 0.003593. The RMSE findings show that each model's mistakes are minimal. Among the five models, the IDM has the largest error, followed closely by ASPFM. The errors of all models calibrated in this study, however, are both controlled within a small range. It is clear that ASPFM retains high accuracy when taking into consideration the effects of multi-vehicle interactions, which are challenging for human drivers to assess.

The accuracy of the separate models appears to have been shown by the RMSE as an indicator; however, this is not reliable enough. The discrepancy between real trajectory estimation and model-based trajectory estimation arises from the fact that the output of the model's prediction must be utilized as input for the subsequent instant. Therefore, the model's predictive efficacy must be evaluated based on the accuracy of continuous prediction in trajectory estimation. During calibration, the total single-step prediction errors of each model are determined through parameter adjustment. However, this difference between the trajectory estimation and the calibration process presents a significant challenge: a model may exhibit high accuracy in single-step prediction, yet produce prediction outputs during trajectory estimation that deviate significantly from the actual value (continuous prediction). Therefore, while a model's accuracy may be judged by its low RMSE, this metric is inadequate for cross-sectional comparison of the accuracy of multiple models.

4.2 Trajectory estimation

We calculated all of the trajectories in NGSIM by vehicle ID to obtain a fair assessment of the trajectory estimation accuracy of various models. Over time, the disparity between each model's trajectory simulation and the actual scenario increases. Specifically, the inaccuracy in trajectory estimation steadily grows as the estimation period lengthens. Although the RMSE values of different models may be comparable during calibration, significant differences in errors emerge when predicting trajectories cumulatively over an extensive time period. The trajectories associated with various objective vehicles often have varying lengths due to the specification of an input node as 5 vehicles. To ensure that the accuracy evaluation of models is not influenced by the forecast duration of the trajectories, the final displacement error rate (FDER) and mean absolute error rate (MAER) are defined, respectively:

$$\mathrm{FDER} = \frac{\mathrm{FDE}}{t} \tag{11}$$

$$\mathrm{MAER} = \frac{1}{n}\sum_{i=1}^{n} \mathrm{FDER}_i \tag{12}$$

where FDER_i stands for the FDER of the ith vehicle and FDE is the final displacement error, which is the expected deviation of the trajectory at the last instant (the moment of collision is the final moment if it coincides with the coordinates of the leading and rear vehicles in the actual trajectory). To counteract the impact of the forecast length, FDER is averaged across the time of FDE. Additionally, the MAER is an average over the FDER of various trajectories Additionally, both measurements have the same units ($\mathrm{m{\cdot}s^{-1}}$ for velocity), which represents the average forecast error per unit of time. All trajectories with a duration longer than 20 s and maximum acceleration of the objective vehicle exceeding 1 $\mathrm{m{\cdot}s^{-2}}$ are selected as candidate trajectories for the trajectory estimation in this paper.

As depicted in Fig. 7, when several models are utilized for the estimate of the specified trajectories, OVM performs the poorest while ASPFM performs the best. Different models deviate differently while forecasting the same trajectory. FVD predicts well overall but performs worse on some specific trajectories. When estimating trajectory, the maximum FDER values of OVM, FVD, IDM, and DRPFM are all beyond the interval of [3 $\mathrm{m{\cdot}s^{-1}}$, −3 $\mathrm{m{\cdot}s^{-1}}$]. The smoothest trajectory estimate was demonstrated by the FDER of the ASPFM, which is entirely regulated to [2 $\mathrm{m{\cdot}s^{-1}}$, −2 $\mathrm{m{\cdot}s^{-1}}$].

The mean absolute error rate (MAER) of each model is derived by averaging the FDER of different models, as shown in Table 3. With an average estimation bias for the trajectory of roughly 0.9 $\mathrm{m{\cdot}s^{-1}}$, it is clear from this statistic that OVM and DRPFM perform the poorest. The MAER of ASPFM is comparable to that of FVD and IDM, both of which hover around 0.5 $\mathrm{m{\cdot}s^{-1}}$. ASPFM, however, still has a minor edge in this area, lowering the error rate by roughly 7% in comparison to FVD which came in second. This is mostly because the front and rear cars in the trajectory prediction tests are using actual data instead of interacting with

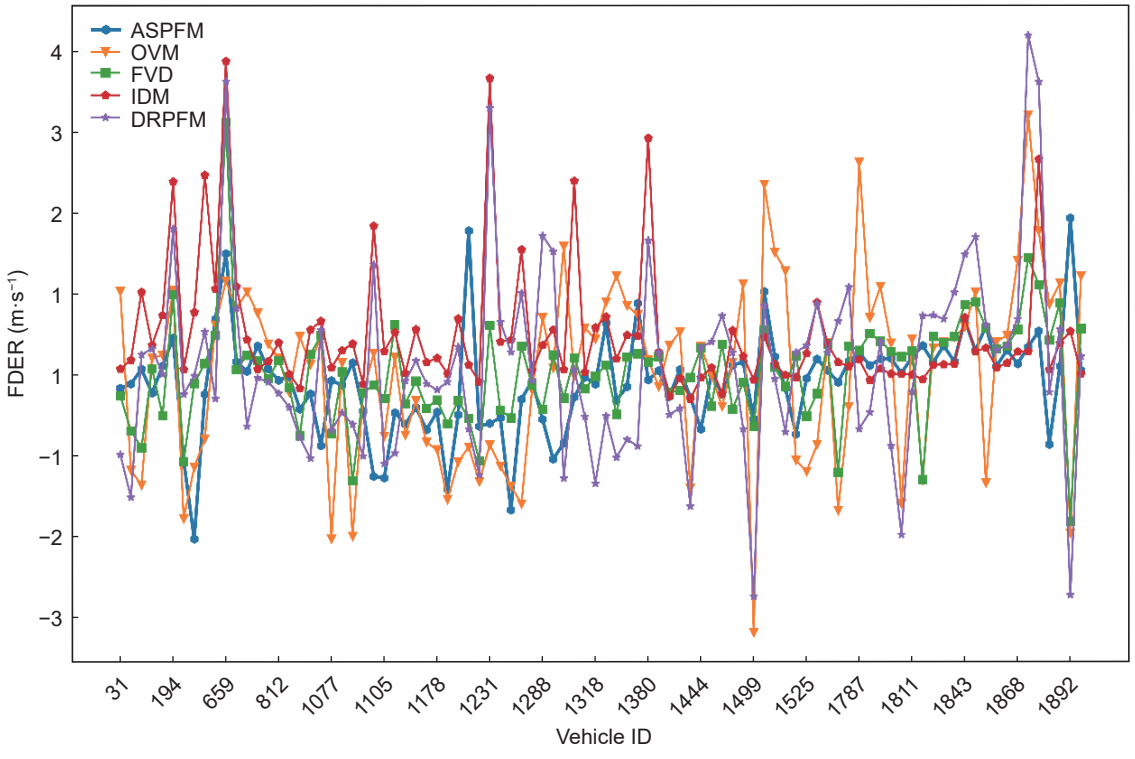

Fig. 7 FDER of different models: FDER of the same model is represented on the same line, and FDER of the same vehicle is represented on the same horizontal coordinate.

Table 3 MAER of different models

Model	ASPFM	OVM	FVD	IDM	DRPFM
MAER (m·s^{-1})	0.440 0	0.914 4	0.474 1	0.523 4	0.843 8

one another. Consequently, there is a possibility of "collision". The full-length trajectory estimate is more favorable for the model that can finish it since the FDER is the average of the deviation of the trajectory endpoints versus time. The schematic representation of the chosen typical trajectory is shown in Figs. 8–11.

OVM and DRPFM performed the worst in trajectory estimation for the vehicle with ID 1440 (the estimation results are depicted in Fig. 8). They were unable to create the proper following spacing in accordance with the status of the leading vehicle, resulting in "collisions" with the rear vehicle at about 10 s.

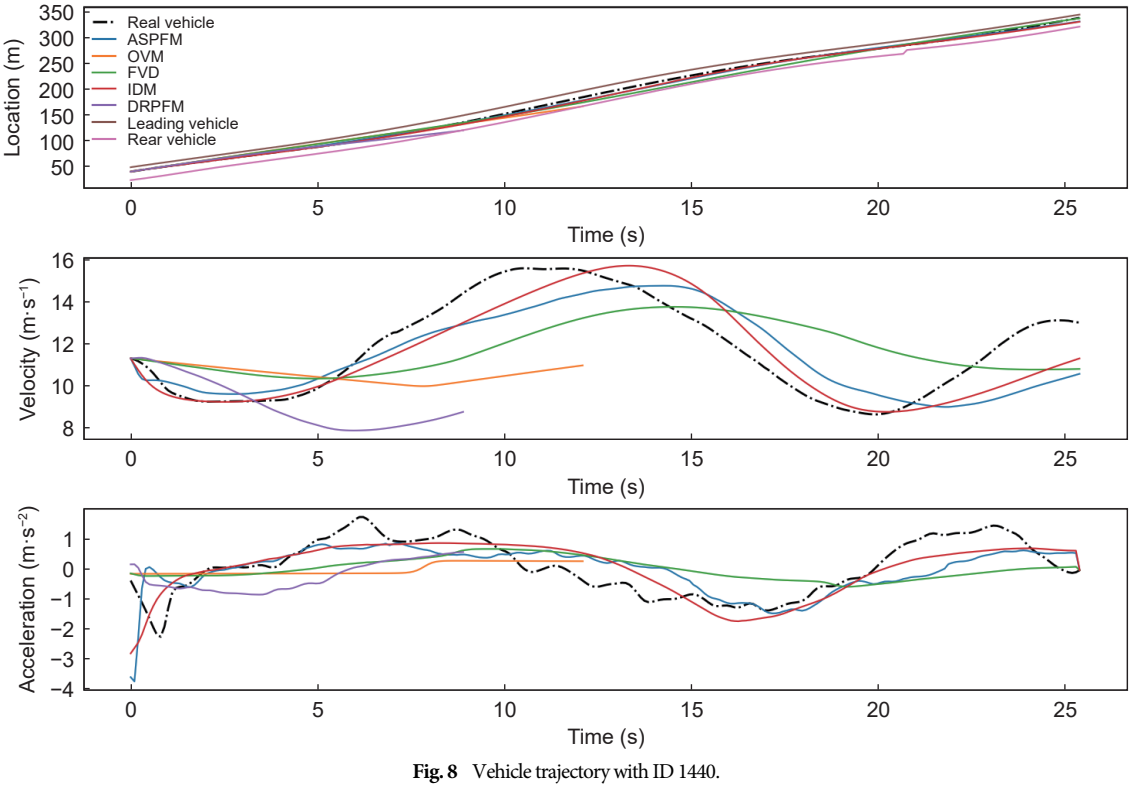

Fig. 8 Vehicle trajectory with ID 1440.

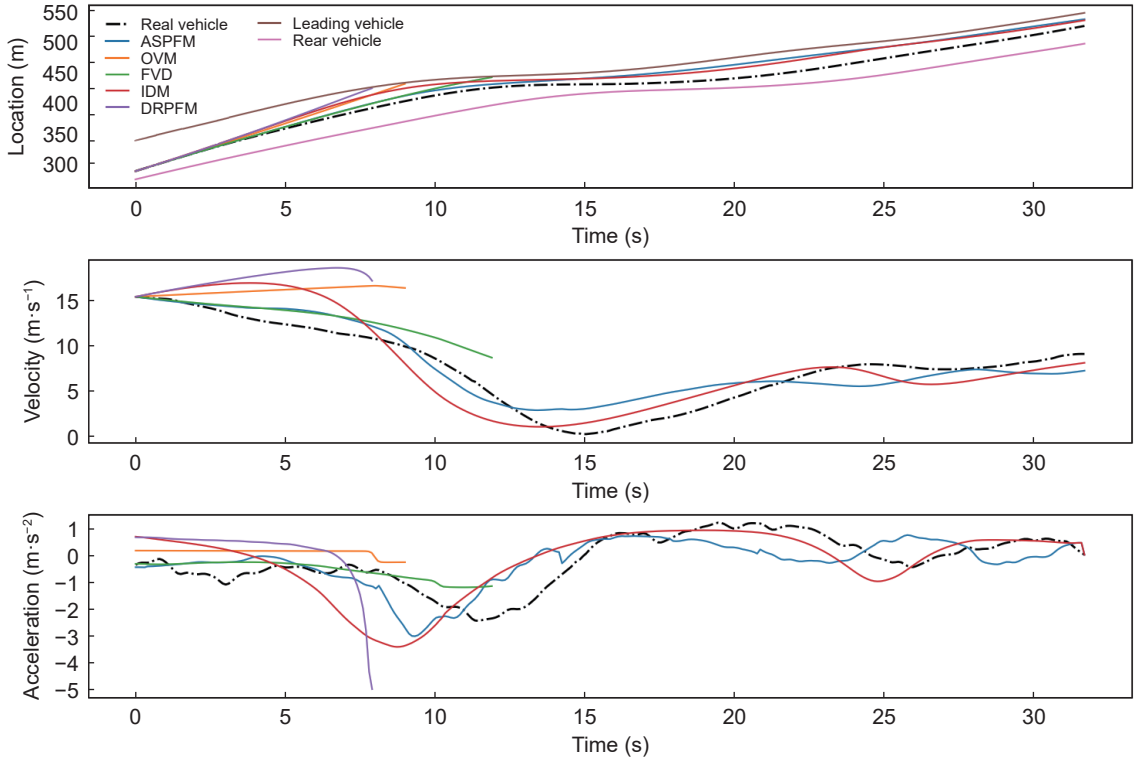

Fig. 9 Vehicle trajectory with ID 1876.

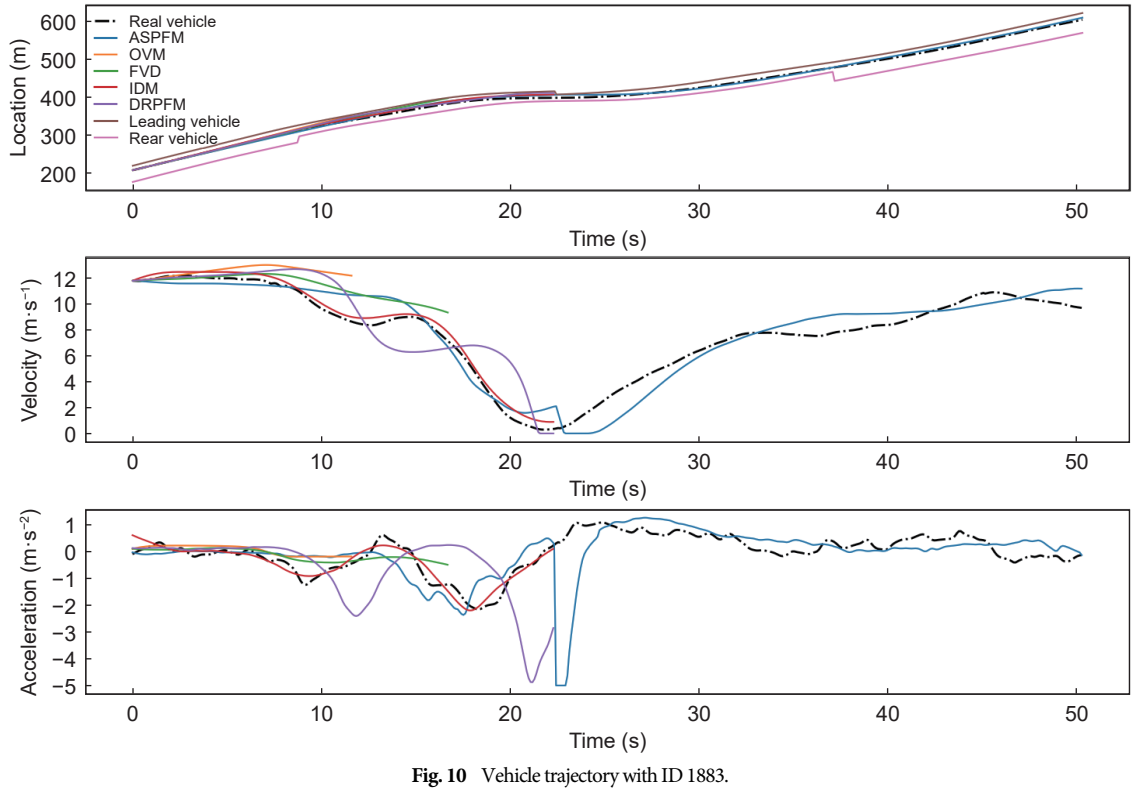

Fig. 10 Vehicle trajectory with ID 1883.

This also contributed to both of them having high FDER. In contrast, the improved trajectory estimate was demonstrated by ASPFM, FVD, and IDM. It is evident that ASPFM and IDM perform in a somewhat comparable manner, which is also consistent with the performance shown in Fig. 7. Similar trajectory estimation capabilities and results are displayed for the identical vehicles by ASPFM and IDM.

As illustrated in Fig. 9, ASPFM and IDM continue to provide accurate trajectory estimates for ID 1876. In contrast, after around 8 s, the leading car was struck by both OVM and DRPFM. Similar to this, FVD did not slow down enough and "struck" the leading car at around 12 s.

Fig. 10 highlights a key distinction between ASPFM and other control strategies implemented in the models. In the trajectory estimation for ID 1888, all other models failed to maintain a safe following distance and subsequently collided with the cut-in

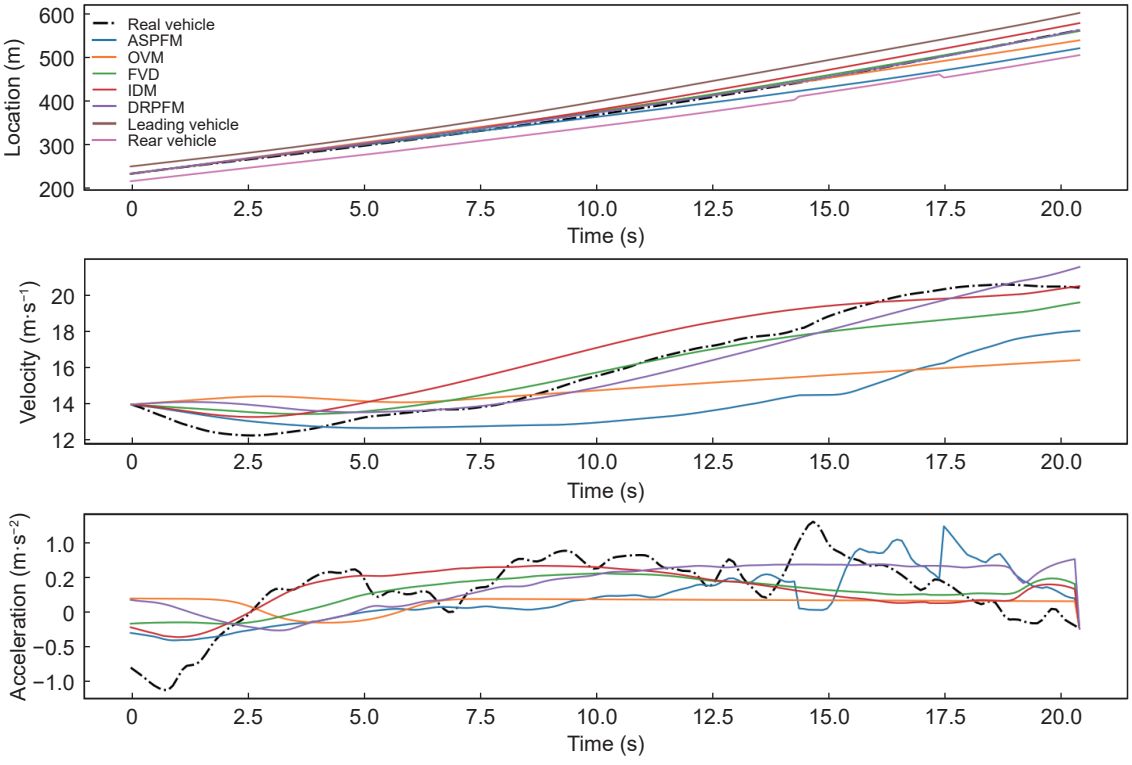

Fig. 11 Vehicle trajectory with ID 380.

vehicle. In contrast, ASPFM demonstrated superior risk analysis in the adjacent lane, ensuring a safe distance from the leading vehicle. Furthermore, ASPFM executed suitable deceleration and autonomously completed the entire trajectory estimation process after the adjacent lane vehicles had cut in.

The trajectory of ID 380 (Fig. 11) demonstrates that all models give a more precise estimate of the trajectory in a more relaxed environment. However, at this point, ASPFM produces a relatively slight deceleration at the final moment because it perceives a lower risk to the rear. For ID 1061, ASPFM has the lowest trajectory estimate accuracy compared to the other models.

In conclusion, ASPFM has a good performance in long-distance trajectory estimation. OVM and DRPFM have insufficient control over the following distance and are not sensitive enough to the state of the leading vehicle, which causes an average trajectory variation of more than 0.84 m/s. Comparatively, the following trajectory can be accurately reproduced by FVD, IDM, and ASPFM. In terms of trajectory estimation, ASPFM performs similarly to IDM, however, when comparing the accuracy of all trajectories combined, ASPFM's MAER is around 16% less accurate than that of IDM.

5 Conclusions

This study suggests a vehicle control approach for the connected and automated vehicle environment that is validated by applying it in the car-following process. When there are moving vehicles in the adjacent lane, it can rationally estimate the acceleration of objective vehicle in the car-following process. As demonstrated in the results, the ASPFM developed in this paper may accomplish comparably reasonable risk quantification and be competent for directing vehicles in car-following processes. The initial values of ASPFM parameters are calibrated and validated based on the NGSIM dataset. When only the influence of the front vehicle is taken into account, the accuracy of some models performs better than ASPFM. However, also based on the NGSIM dataset for parameter calibration, other models can even experience collisions with the vehicle in front. ASPFM can make a comprehensive decision on whether to adjust the speed to drive on the path of least risk based on the state of surrounding cars. As a result, the unanticipated circumstance of rear-end pursuing can be avoided. This paper introduces avoidance coefficients that can characterize the tendency for the outside lane to avoid and the inside lane to accelerate when driving alongside each other. We also proposed goal force and lane resistance to allow vehicles to start from rest in the theoretical system of potential field virtual forces.

By calibrating with a substantial amount of data from a single driver, ASPFM is capable of exhibiting similar characteristics as that of the driver, which enables it to better meet the driver's requirements by aligning with their driving habits. The potential field model in this research can describe the effect of special vehicles because it can reflect the anisotropy of vehicle influence. To achieve an amplified effect from special vehicles, for instance, the bulk of vehicles such as police vehicles and ambulances can be increased. When calculating the impact of the special vehicle on ordinary vehicles using this model, lower the v_m of the special vehicle to increase its x-axis positive influence to accomplish the effect of the special vehicle causing the vehicle ahead to speed up the lane or avoid it. In the future, connected and automated vehicles will be capable of modeling the entire traffic environment, serving as a foundation for the vehicle's acceleration determination. The potential field model used in this study assumes uniformity of the entire traffic environment and all characteristics analyzed are in global coordinate systems. The model is effective in representing possible new traffic environments and evaluating their impact on the objective vehicle, particularly in complex traffic scenarios. The fundamental idea behind the concept is that, by utilizing vehicle following as a benchmark, the effect of a new transportation element could be translated and reduced to a separate "leading vehicle" with a varied range, size, and principle of action. In other words, the complexity of modeling environmental elements can be effectively

reduced, and long-tail scenarios can be effectively solved, by first using the potential field to describe a conventional scene and then modeling the actual effect of the potential field on complex traffic environment elements.

Nevertheless, ASPFM has some significant flaws that need further work. First, ASPFM does not take into account the fact that human-like driving behavior has been the subject of scholarly attention (Huang et al., 2022). A feature of human-like driving research is that diverse road users communicate with each other. From this perspective, the model put out in this research wastes the ability of linked smart vehicles to communicate and make decisions. Even though this work employs multiple vehicles in the same lane for parameter calibration, a significant amount of data from the same driver is required to correctly calibrate the model parameters. A data collection experiment should be planned to make the parameter values of ASPFM more realistic. The driver in this experiment is constantly informed of the state of the nearby obstacle vehicles and able to perceive risk appropriately and make decisions based on these conditions. The vehicle control model proposed in this paper can only be fully sensible and even human-like in this way.

Replication and data sharing

Next Generation Simulation (NGSIM) is available at: https://ops.fhwa.dot.gov/trafficanalysistools/ngsim.htm.

Acknowledgements

This research was sponsored by the National Key R&D Program of China (Grant No. 2018YFB160220600), MOE (Ministry of Education in China) Project of Humanities, National Natural Science Foundation of China (Grant No. 52202408), and Social Sciences23 (Project No. 20YJAZH083).

Declaration of competing interest

The authors declare that they have no known competing financial interests or personal relationships that could have appeared to influence the work reported in this paper.

References

Arun, A., Haque, M. M., Washington, S., Mannering, F., 2023. A physics-informed road user safety field theory for traffic safety assessments applying artificial intelligence-based video analytics. Anal Methods Accid Res, 37, 100252.

Cheng, Z., Yuan, J., Yu, B., Lu, J., Zhao, Y., 2022. Crash risks evaluation of urban expressways: A case study in Shanghai. IEEE Trans Intell Transp Syst, 23, 15329–15339.

Fu, L. M., Fu, Y. F., 2005. Numerical simulation on characteristics of turbulent flow around two cars driving side-by-side. Journal of Jilin University (Engineering and Technology Edition), 35, 358–362. (in Chinese)

Gipps, P. G., 1981. A behavioural car-following model for computer simulation. Transp Res B Methodol, 15, 105–111.

Gunay, B., 2007. Car following theory with lateral discomfort. Transp Res B Methodol, 41, 722–735.

Huang, Y., Ding, H., Zhang, Y., Wang, H., Cao, D., Xu, N., *et al*., 2020. A motion planning and tracking framework for autonomous vehicles based on artificial potential field elaborated resistance network approach. IEEE Trans Ind Electron, 67, 1376–1386.

Huang, Z., Wu, J., Lv, C., 2022. Driving behavior modeling using naturalistic human driving data with inverse reinforcement learning. IEEE Trans Intell Transp Syst, 23, 10239–10251.

Jiang, R., Wu, Q., Zhu, Z., 2001. Full velocity difference model for a car-following theory. Phys Rev E, 64, 017101.

Jiao, S., Zhang, S., Zhou, B., Zhang, L., Xue, L., 2021. Dynamic performance and safety analysis of car-following models considering collision sensitivity. Phys A Stat Mech Appl, 564, 125504.

Khatib, O., 1986. Real-time obstacle avoidance for manipulators and mobile robots. Int J Robot Res, 5(1), 90–98.

Khattak, A. J., Ahmad, N., Wali, B., Dumbaugh, E., 2021. A taxonomy of driving errors and violations: Evidence from the naturalistic driving study. Accid Anal Prev, 151, 105873.

Kim, Y., Onesto, L., Tay, S., Yang, L., Guanetti, J., Savaresi, S., *et al*., 2020. Shared Perception for Connected and Automated Vehicles. In: 2020 IEEE Intelligent Vehicles Symposium (IV), Las Vegas, NV, USA, 21–26.

Kometani, E., Sasaki, T., 1959. Dynamic behaviour of traffic with a nonlinear spacing-speed relationship. In: Proceedings of the Symposium on Theory of Traffic Flow, 105–119.

Lee, D. N., 1976. A theory of visual control of braking based on information about time-to-collision. Perception, 5, 437–459.

Li, L., Chen, X., 2017. Vehicle headway modeling and its inferences in macroscopic/microscopic traffic flow theory: A survey. Transp Res C Emerg Technol, 76, 170–188.

Li, L., Gan, J., Ji, X., Qu, X., Ran, B., 2022. Dynamic driving risk potential field model under the connected and automated vehicles environment and its application in car-following modeling. IEEE Trans Intell Transp Syst, 23, 122–141.

Li, L., Gan, J., Yi, Z., Qu, X., Ran, B., 2020a. Risk perception and the warning strategy based on safety potential field theory. Accid Anal Prev, 148, 105805.

Li, L., Gan, J., Zhou, K., Qu, X., Ran, B., 2020b. A novel lane-changing model of connected and automated vehicles: Using the safety potential field theory. Phys A Stat Mech Appl, 559, 125039.

Liu, X., Wang, Y., Jiang, K., Zhou, Z., Nam, K., Yin, C., 2022. Interactive trajectory prediction using a driving risk map-integrated deep learning method for surrounding vehicles on highways. IEEE Trans Intell Transp Syst, 23, 19076–19087.

Lyu, N. C., Wang, Y. G., Wu, C. Z., Peng, L. F., Thomas, A. F., 2022. Using naturalistic driving data to identify driving style based on longitudinal driving operation conditions. J Intell Connect Veh, 5, 17–35.

Mac, T. T., Copot, C., Tran, D. T., De Keyser, R., 2016. Heuristic approaches in robot path planning: A survey. Robotics Auton Syst, 86, 13–28.

Masmoudi, M., Friji, H., Ghazzai, H., Massoud, Y., 2021. A reinforcement learning framework for video frame-based autonomous car-following. IEEE Open J Intell Transp Syst, 2, 111–127.

Noto, N., Okuda, H., Tazaki, Y., Suzuki, T., 2012. Steering assisting system for obstacle avoidance based on personalized potential field. In: 15th International IEEE Conference on Intelligent Transportation Systems, Anchorage, AK, USA. IEEE, 1702–1707.

Perera, L. P., Guedes Soares, C., 2015. Collision risk detection and quantification in ship navigation with integrated bridge systems. Ocean Eng, 109, 344–354.

Rasekhipour, Y., Khajepour, A., Chen, S. K., Litkouhi, B., 2017. A potential field-based model predictive path-planning controller for autonomous road vehicles. IEEE Trans Intell Transp Syst, 18, 1255–1267.

Tan, H., Lu, G., Liu, M., 2022. Risk field model of driving and its application in modeling car-following behavior. IEEE Trans Intell Transp Syst, 23, 11605–11620.

Wang, J., Wu, J., Li, Y., 2015. The driving safety field based on driver–vehicle–road interactions. IEEE Trans Intell Transp Syst, 16, 2203–2214.

Wang, J., Wu, J., Zheng, X., Ni, D., Li, K., 2016. Driving safety field theory modeling and its application in pre-collision warning system. Transp Res C Emerg Technol, 72, 306–324.

Wang, L., Abdel-Aty, M., Ma, W., Hu, J., Zhong, H., 2019. Quasi-vehicle-trajectory-based real-time safety analysis for expressways. Transp Res C Emerg Technol, 103, 30–38.

Wang, W., Wang, W., Wan, J., Chu, D., Xu, Y., Lu, L., 2019. Potential field based path planning with predictive tracking control for autonomous vehicles. In: 5th International Conference on Transportation Information and Safety (ICTIS), Liverpool, UK. IEEE, 746–751.

Xing, H., Liu, Y., 2022. Graph attention network for Car-Following Model under game between desired and real state. IET Intell Transp Syst, 16, 800–812.
Xu, Q., Li, K., Wang, J., Yuan, Q., Yang, Y., Chu, W., 2022. The status, challenges, and trends: an interpretation of technology roadmap of intelligent and connected vehicles in China (2020). J Intell Connect Veh, 5, 1–7.
Xu, Z., Fang, Y., Zheng, N., & Vu, H. L., 2022. Analyzing the inconsistency in driving patterns between manual and autonomous modes under complex driving scenarios with a VR-enabled simulation platform. J Intell Connect Veh, 5, 215–234.
Yang, M., Wang, X., Quddus, M., 2019. Examining lane change gap acceptance, duration and impact using naturalistic driving data. Transp Res C Emerg Technol, 104, 317–331.
Yu, W., Lu, Y., 2021. UAV 3D environment obstacle avoidance trajectory planning based on improved artificial potential field method. J Phys: Conf Ser, 1885, 022020.
Yuan, Q., Xu, X., Wang, T., Chen, Y., 2022. Investigating safety and liability of autonomous vehicles: Bayesian random parameter ordered probit model analysis. J Intell Connect Veh, 5, 199–205.
Zhao, H., Rao, G., 2021. Traffic Accident Prediction Methods Based on Multi-factor Models. In: International Conference on Knowledge Science, Engineering and Management. Cham: Springer, 41–52.
Zhao, X., He, R., Wang, J., 2020. How do drivers respond to driving risk during car-following? Risk-response driver model and its application in human-like longitudinal control. Accid Anal Prev, 148, 105783.
Zheng, X., Huang, B., Ni, D., Xu, Q., 2018. A novel intelligent vehicle risk assessment method combined with multi-sensor fusion in dense traffic environment. J Intell Connect Veh, 1, 1–14.
Zhu, Jie, Easa, S., Gao, Kun., 2022. Merging control strategies of connected and autonomous vehicles at freeway on-ramps: A comprehensive review. J Intell Connect Veh, 5, 99–111.
Zhu, M., Wang, X., Wang, Y., 2018. Human-like autonomous car-following model with deep reinforcement learning. Transp Res C Emerg Technol, 97, 348–368.

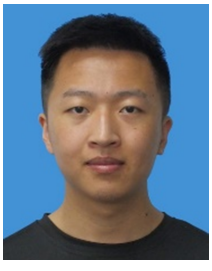

Haozhan Ma received his B.E. degree from Southeast University, China, in 2021. He is currently pursuing his M.S. degree with the Research Center for Internet of Mobility, Southeast University. His main research interests include the research of connected and automated vehicles.

Bocheng An received his B.E. degree from Southeast University, China, in 2021. He is currently pursuing his M.S. degree with the Research Center for Internet of Mobility, Southeast University. His main research interests include traffic prediction and traffic control.

Linheng Li received his Ph.D. degree from Southeast University, Nanjing, China, in 2017. He is currently a postdoctoral fellow with the Research Center for Internet of Mobility, Southeast University. His research interests include connected and automated vehicles, road traffic safety, traffic control and management, and traffic flow theory.

Zhi Zhou received his M.S. degree from Purdue University, USA. He is currently pursuing his Ph.D. degree with the Research Center for Internet of Mobility, Southeast University. His research interests include the research of connected and automated vehicles and vehicle-road cooperative autonomous driving.

Xu Qu received his Ph.D. degree from Southeast University, Nanjing, China, in 2013. He is currently an Associate Professor with the School of Transportation, Southeast University; the Vice Dean of the Joint Research Institute on Internet of Mobility, founded by Southeast University, China; and the University of Wisconsin-Madison, USA. His research interests include connected automated vehicle highway systems, intelligent transportation systems, and traffic control and management.

Bin Ran received his Ph.D. degree from the University of Illinois at Chicago, USA, in 1993. He is currently a Professor with the Department of Civil and Environmental Engineering, University of Wisconsin-Madison, WI, USA, and the Director of the Research Center for Internet of Mobility, Southeast University, Nanjing, China. He has authored or coauthored more than 90 articles on international journals, including *Transportation Science*, *Transportation Research Part B*, and *Transportation Research Part C*. He is one of the cofounders of Chinese Overseas Transportation Association (COTA), and he was the first Chairman.